Materials Science and Engineering A 528 (2011) 2736–2747

Contents lists available at ScienceDirect

Materials Science and Engineering A

journal homepage: www.elsevier.com/locate/msea

Microstructure modifications induced by a laser surface treatment in an AA7449 aluminium alloy

G. Fribourg[a], A. Deschamps[a,*], Y. Bréchet[a], G. Mylonas[b], G. Labeas[b], U. Heckenberger[c], M. Perez[d]

[a] SIMAP, INPGrenoble-CNRS-UJF, BP 75, 38402 St Martin d'Hères Cedex, France
[b] Laboratory of Technology and Strength of Materials (LTSM), Department of Mechanical Engineering and Aeronautics, University of Patras, Panepistimioupolis, Rion, 26500 Patras, Greece
[c] EADS Deutschland GmbH, EADS Innovation Works, IW-MS, 81663 Munich, Germany
[d] Université de Lyon, INSA Lyon, MATEIS, UMR CNRS 5510, 7, avenue Jean-Capelle, 69621 Villeurbanne Cedex, France

ARTICLE INFO

Article history:
Received 22 October 2010
Received in revised form 6 December 2010
Accepted 6 December 2010
Available online 10 December 2010

Keywords:
Laser surface treatment
Al–Zn–Mg–Cu
Precipitation
Modelling

ABSTRACT

This work investigates the modification of the precipitate microstructure induced by laser surface treatments in an AA7449 aluminium alloy in T7651 temper. Microhardness maps in the cross-section below the laser lines, as well as maps of the precipitate size and volume fraction obtained by Small-Angle X-ray Scattering, show that a significant precipitate dissolution and coarsening has been induced by the laser treatment. Integrated modelling is carried out to quantify this effect, including a thermal finite element model, a size class precipitation model and a precipitation hardening model. The precipitation model is calibrated using separate reversion experiments, and then coupled to the thermal and mechanical models, allowing a quantitative description of the modification of the microstructure.

1. Introduction

Laser surface treatments for aluminium alloys have experienced extensive development in the past 10 years, aiming at modifying the shape and properties of aluminium components, particularly in the aerospace industry. Three types of laser treatments have emerged as practically viable. The first is Laser Shock Peening (LSP), sometimes simply called Laser Peening [1–8]. It consists of sending very short athermal laser pulses (a few tens of ns) that induce a shock wave in the material and result in significant compressive surface internal stresses, which may notably improve the fatigue resistance of the alloys. The second is Laser Surface Melting, which aims at melting a small depth of the alloy (typically 10–300 μm) in order to obtain a solute-rich microstructure and improve the stress corrosion cracking performance of the material [9,10].

A third technique, which has received less attention, is Laser Beam Forming, which uses the laser operation as a tool for modifying the component shape, by the plastic flow that follows the non-uniform thermal dilatation of the material [11–15]. Such treatments, where the material stays in the solid state, provide an attractive solution for correcting the distortion of aerospace components, which is often found in thin walls after machining of thick plates, due to the presence of quench induced internal stresses [16].

Laser Beam Forming (LBF) is a complex process, where the shape modification of the alloy is the result of highly inhomogeneous, non-isothermal temperature paths, and depends in detail on the thermo-mechanical response of the material in a wide range of temperatures and strain rates. The temperature field induced by such laser treatments has been modelled by Hu and co-workers [13] and Ji and Wu [11]. More recently, Labeas [15] has included the mechanical response of the material to reach a thermo-mechanical description of the process. However there is little evaluation in the literature of the effect that this laser treatment may have on the alloy's fine scale microstructure, and on the related in-use properties. Chan and Liang [12] and Geiger and co-workers [14] have reviewed the influence of LBF on microstructure in aluminium alloys of the 6000 series (AA6013 and AA6082). They indicate changes in dislocation density, grain structure, and precipitate structure. No study is available on the microstructure modifications in 7000 series aluminium alloys, although they are direct potential candidates for part distortion correction in aerospace components.

High strength 7000 series aluminium alloys gain their mechanical properties essentially by precipitation hardening [17]. It is known that the precipitates present in peak strength tempers of these alloys are very sensitive to a sudden heat input, which can be for instance met in MIG welding [18], friction stir welding [19] or electron beam welding [20]. Due to the sudden increase of tempera-

---

* Corresponding author.
E-mail address: alexis.deschamps@simap.grenoble-inp.fr (A. Deschamps).

0921-5093/$ – see front matter © 2010 Elsevier B.V. All rights reserved.
doi:10.1016/j.msea.2010.12.018

ture, precipitates can either be dissolved or experience coarsening, and this can be adequately described by appropriate modelling of non-isothermal precipitation kinetics [21].

Characterising the evolution of the nanoscale precipitation state during non isothermal, non homogeneous heat treatments requires the use of tools which make it possible to perform microstructure mapping, and which can be performed in situ during customised heat treatments. Small-Angle X-ray Scattering (SAXS), particularly when performed with a synchrotron source, is a characterisation technique compatible with these requirements [22]. It provides a quantitative measure of precipitate size and volume fraction, can be applied to microstructure mapping with a spatial resolution typically in the range of 200 μm, and can be performed during rapid non isothermal temperature paths.

The aim of the present paper is first to provide a quantitative assessment by SAXS of the microstructure changes and related microhardness distribution due to laser treatments performed on plates of the high strength AA7449 alloy in the T7651 temper. In order to make the problem simpler, the laser treatments will be performed on relatively thick plates (5 mm), in order to minimise the sample deformation and therefore to study mainly the thermal processes related to the laser treatment.

Secondly, SAXS measurements carried out during reversion experiments (rapid heating of the alloy to a prescribed temperature) will be performed in situ to assess the material response to sudden temperature changes. A combined thermal and microstructure model will then be used to predict the microstructure after the laser treatment. The model parameters will be adjusted to the reversion treatments and then applied on the temperature fields predicted by the thermal model. A simple model for precipitation hardening will then be applied to the predicted microstructure maps and compared to the experimental hardness maps.

2. Materials and experimental methods

The studied material is an AA7449 alloy, a wrought aluminium alloy of the Al–Zn–Mg–(Cu) family. The specific composition of the received plate, provided by Alcan – Centre de Recherches de Voreppe (France), was 8.3% zinc, 2.2% magnesium and 1.9% copper (all in wt%). The as-received temper was T7651, i.e. pre-strained and over-aged. The industrial ageing treatment consists in a water quench from the solution treatment temperature, a plastic deformation of about 2%, a few days of natural ageing, and a two step ageing treatment: 6 h at 120 °C and 10 h at 160 °C.

The laser treatment was applied on the Long/Short Transverse plane of rolled plates of dimension 170 × 76 × 5 (mm). Five consecutive laser lines were performed with a diode pumped solid state Nd:YAG laser ($\lambda = 1064$ mm), as shown in Fig. 1, in order to investigate the effect of plate heating when repeating the process. At the end of the first four lines the laser was shut off for 10 s to allow for a distribution of the heat within the plate before proceeding with the subsequent line. The beam was defocused to a diameter of 5 mm, the beam power was 3000 W and the velocity of the beam was 10 mm/s. Within about 3 s after the last line was finished, the samples were kept in liquid nitrogen until further investigation to prevent any evolution of the microstructure.

Hardness maps were performed on mirror polished surfaces using a semi-automatic micro-indenter with a weight of 100 g. Hardness line-scans across the lines on the plate surface (slightly polished) gave access to the properties of the outermost surface, while cross-section maps gave access to the in-depth hardness evolution.

Mapping of the precipitate microstructure in the laser treated material was achieved using Small-Angle X-ray Scattering. Slices parallel to the plate surface and of thickness 100 μm were prepared by cutting and mechanical polishing. Line scans were then performed on these slices across the laser line while recording the SAXS images with a CCD camera. X-ray measurements were performed on the D2AM/BM02 beamline of the European Synchrotron Radiation facility (ESRF), at a wavelength of 1.3 Å. The accessible range of scattering vectors was [0.007–0.4] Å^{-1}, and the beam diameter was 200 μm. CCD camera data was corrected for readout noise, distortion, flat-field, background noise. It was normalised using a reference sample and transmission measurements through calibrated filters.

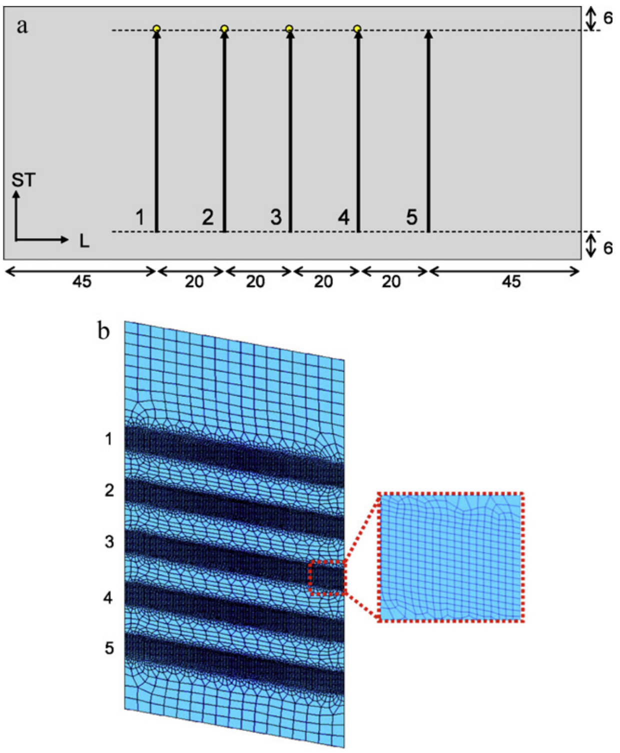

Fig. 1. (a) Scheme of the 5 laser lines realised on the AA7449 plates (units are in mm); the circles indicate a pause of 10 s to distribute the heat within the plate before proceeding. (b) Scheme of the FE mesh for thermal modelling.

Reversion experiments were also carried out while measuring in situ the SAXS images. Samples of originally T7651 temper material were inserted in a rapid heating furnace and heated in the range of 200–400 °C with a heating rate of 10 °C s^{-1}. SAXS recordings were made every 5 s during these heat treatments.

3. Results: hardness maps

Fig. 2 shows the hardness maps realised on the lines #1, 3 and 5. Fig. 3 shows in more detail the hardness profiles for the same lines. The "top" labelled line was measured on the plate surface after slight mechanical polishing. The other lines were measured on the plate cross-section.

From these measurements, the heat-affected zone, as defined by the zone where the hardness is affected as compared to the base material, can be evaluated to approximately 4–5 mm wide, namely comparable to the beam size. It is approximately 500 μm deep. In this HAZ, the hardness drops by up to 65 HV. The hardness drop is monotonous as a function of the distance with respect to the beam centre.

The three lines show qualitatively the same behaviour. However, one can observe that when going from the 1st line to the line #5, the minimum drop in hardness is slightly more pronounced.

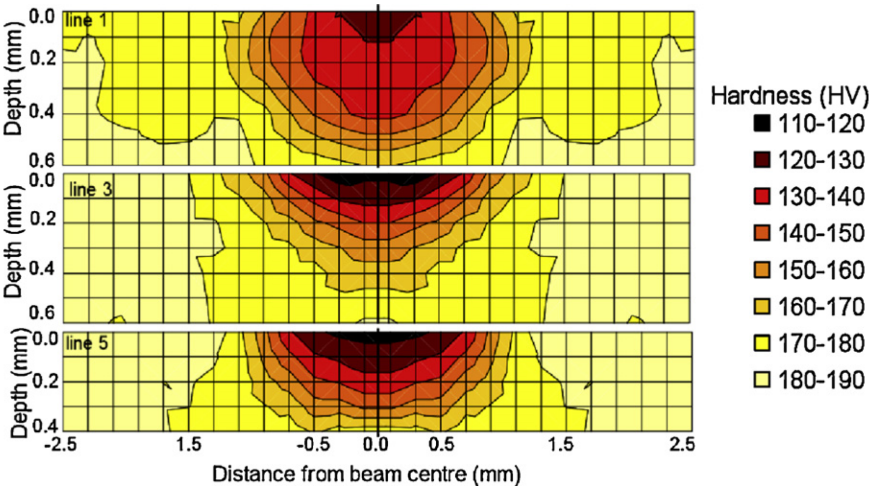

Fig. 2. Microhardness maps of the cross sections below the surface of lines 1 (top), 3 (middle) and 5 (bottom). Note that the longitudinal and vertical scales are different.

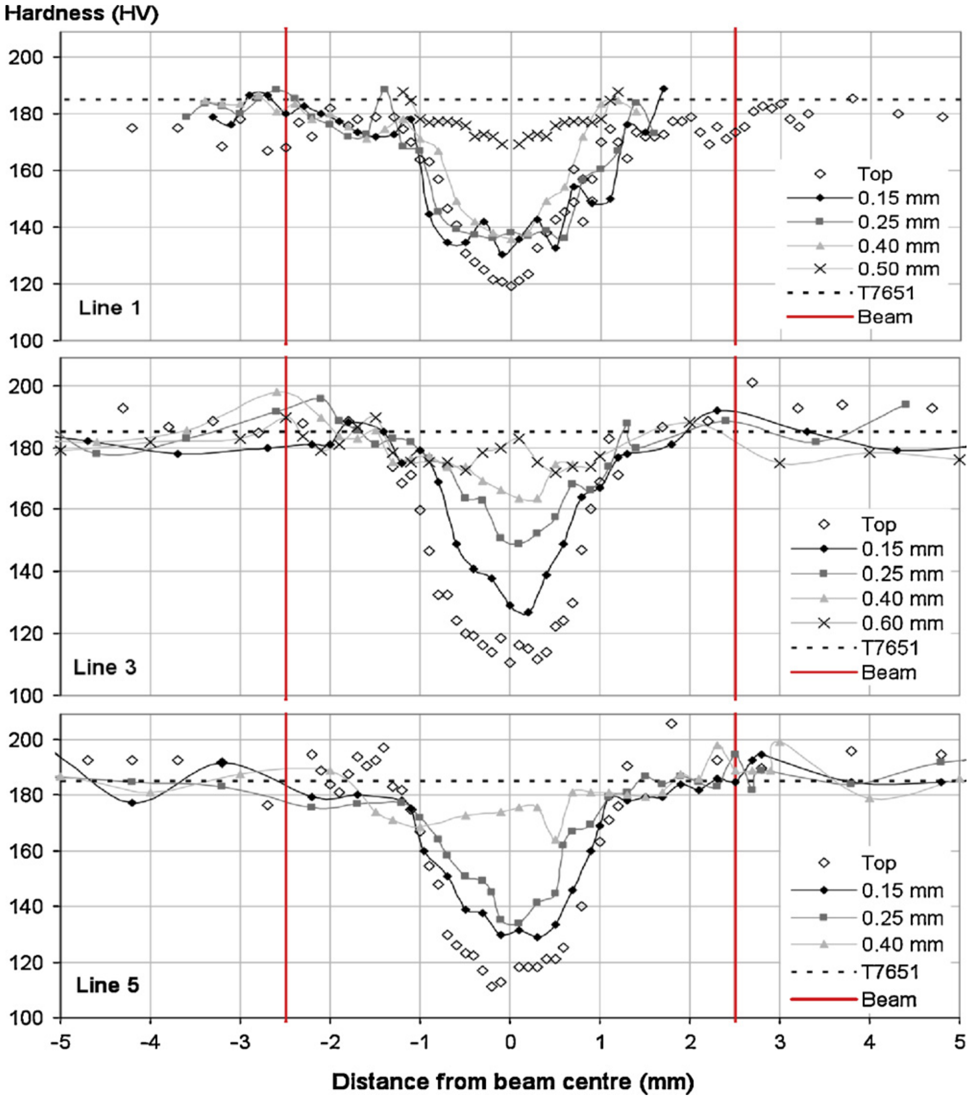

Fig. 3. Hardness profiles realised at different depths below the sample surface for the lines #1, 3 and 5.

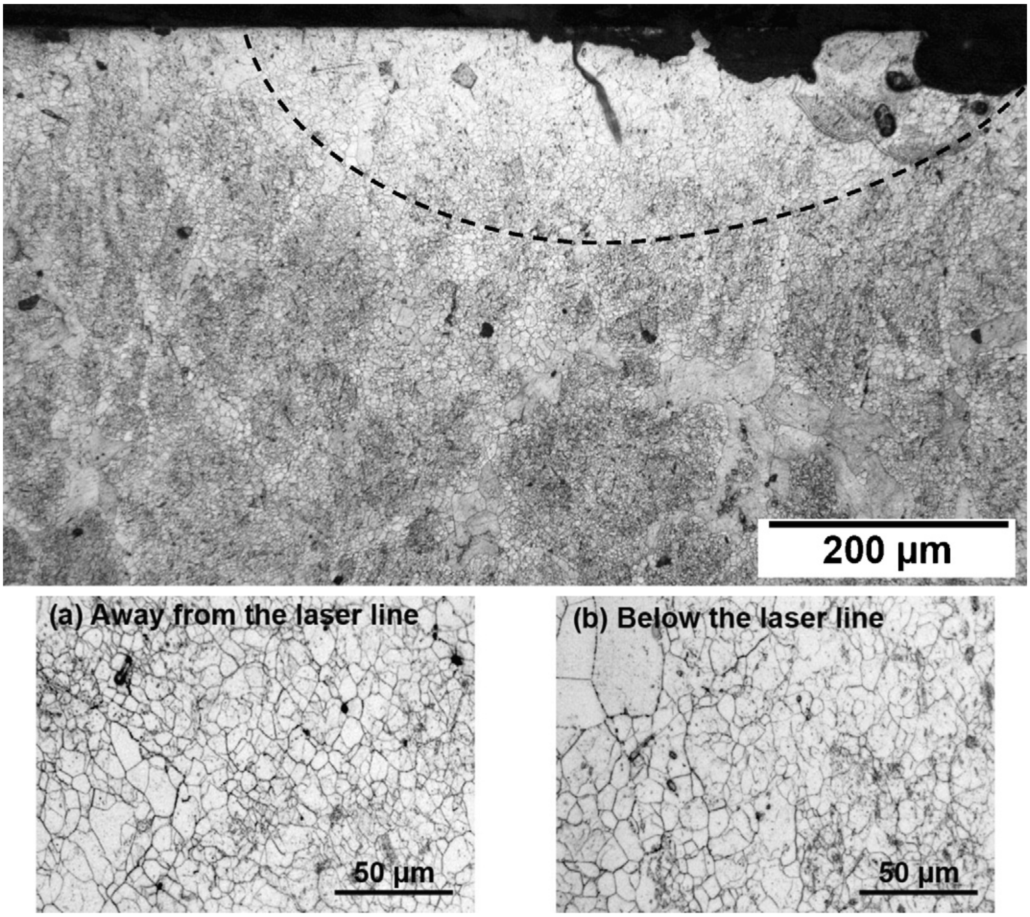

Fig. 4. Optical micrograph after etching in orthophosphoric acid of the area below laser line #3. The dashed line denotes the extension of the zone where precipitate loss is visible on the optical micrograph. The details in figures (a) and (b) show with higher magnification the subgrain structure, and evidence that no significant grain structure variation has occurred immediately below the laser line.

4. Results: measurement of precipitate microstructures

First, we evaluated the possible changes in grain structure that could be induced by the laser treatment. Fig. 4 shows an optical micrograph of the cross-section below the laser line #3, after mirror polishing followed by immersion in warm orthophosphoric acid solution (which reveals the coarse precipitates in 7000 series Al alloys). The micrograph shows that the grain structure is kept unchanged in all the cross-section, and evidences that no melting has occurred due to the laser treatment. The irregular nature of the surface is actually due to milling grooves that were present before the laser treatment. These grooves appeared visually identical after the laser treatment. The optical image of the cross section is lighter below the laser, which indicates that substantial precipitate dissolution has happened. This is further evidenced by observations in Scanning Electron Microscopy (Fig. 5), which evidence that the intergranular and inter-sub-granular precipitates are similar in the material below the laser beam and far away from it. Since no melting or change in grain structure has been detected, and no significant shape change has been recorded, the laser process can be simplified to a purely thermal process involving changes in the precipitate microstructure.

Small Angle Scattering spectra have been interpreted in terms of mean precipitate size using the Guinier radius and in terms of precipitate volume fraction using the measured integrated intensity, similarly to [23]. Fig. 6 shows two examples of scattering curves, one for the base T7651 material, and the other in the heat-affected zone. The precipitates in the HAZ are observed to be present in much lower volume fraction, and somewhat larger precipitate size, as compared to the base material. Fig. 7 shows the line scans corresponding to different depths below the plate surface for the line #3. The heat-affected zone is characterised by a pronounced decrease in precipitate volume fraction up to almost full dissolution 100 µm below the plate surface. This dissolution comes together with a significant increase in precipitate size: the radius in the base material is 52 Å, and goes up to 80 Å just below the beam centre, 100 µm below the sample surface. Note that contrarily to the hardness measurements, it was not possible to obtain SAXS measurements right on the sample surface.

Now the microstructure and hardness maps can be compared with each other. Fig. 8 shows the hardness and volume fraction maps together. It is observed that the two maps fit well together in terms of spatial extension of the HAZ.

5. Results: reversion heat treatments

Reversion treatments were carried out on the T7651 base material in order to provide a quantitative basis for understanding the material response to a sudden rise of temperature. Two types of reversion treatments were carried out: a sudden temperature increase to the prescribed temperature, which was varied from 200 °C to 400 °C, and ramp heat treatments at 0.8 and 1.6 $^\circ\mathrm{C\,s^{-1}}$. Fig. 9 shows the evolution of the volume fraction and precipitate radius during the reversion experiments. As previously observed in similar cases (see e.g. [21]), the reversion

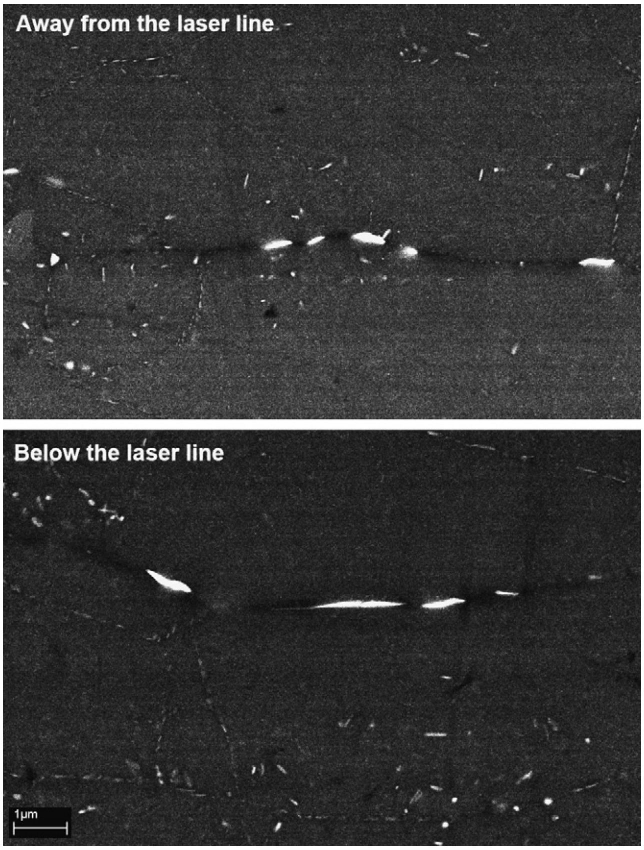

Fig. 5. Field-Emission Gun Scanning Electron micrographs (in-lens BSE detector) of the material immediately below the laser line as compared to the base material, showing that no significant change in grain microstructure and coarse precipitation has occurred.

behaviour consists in a fast drop of volume fraction followed by a slower recovery to reach the equilibrium volume fraction at the temperature of the reversion treatment. During this slow recovery of the volume fraction, extensive precipitate coarsening is observed to happen. When the temperature of the heat treatment increases, both the drop in volume fraction and the increase in volume fraction are more pronounced. The ramp heating results will be presented in the next section along with the modelling results.

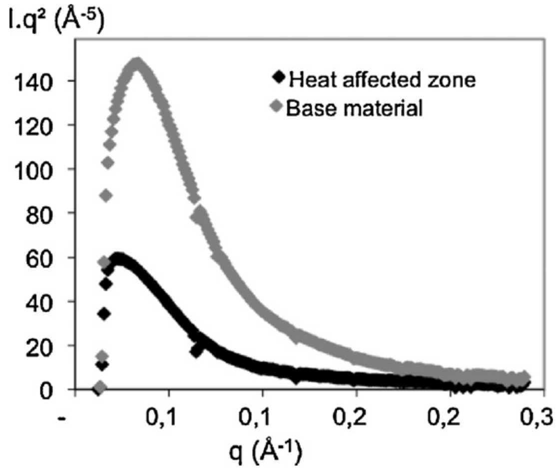

Fig. 6. Two examples of SAXS Kratky plots ($I{\cdot}q^2$ vs. q, where q is the scattering vector) within the laser heat-affected zone and from the base material. The change in intensity indicates the dissolution (lowering of area under the curves) and the increase in radius (shift towards smaller q-values) due to the laser process.

6. Modelling the evolution of precipitates

Reversion experiments coupled with a class precipitation model have been recently shown [24] to be a powerful tool to tune independently the main physical parameters for the precipitation process in a material, such as the solubility product, the interfacial energy and the diffusion constant of the limiting diffusing species.

In this study we used the PreciSo model developed by Perez and co-workers [25] and previously applied to a variety of microalloyed steels. For the details about the model implementation refer to [26].

The initial material consists of a T7651 overaged state, with relatively large precipitates that have a radius of about 5 nm. Therefore, it can be safely assumed that this initial material mostly contains the equilibrium η phase, and that this equilibrium phase will remain the dominant one upon increasing the temperature. Although this phase is well known to contain both Cu and Al atoms, for the sake of simplicity it was assumed here that the material was pseudo-ternary (i.e. Cu atoms were counted as Zn atoms) and that the precipitate composition was $MgZn_2$. The thermodynamics of this phase in the Al matrix was simply described by a solubility product, taking into account the size dependent Gibbs Thomson correction:

$$X^{i}_{\mathrm{Mg}} X^{i2}_{\mathrm{Zn}} = K_{\mathrm{MgZn_2}}(R) = K^{\infty}_{\mathrm{MgZn_2}} \exp(R_{\mathrm{o}}/R) \qquad (1)$$

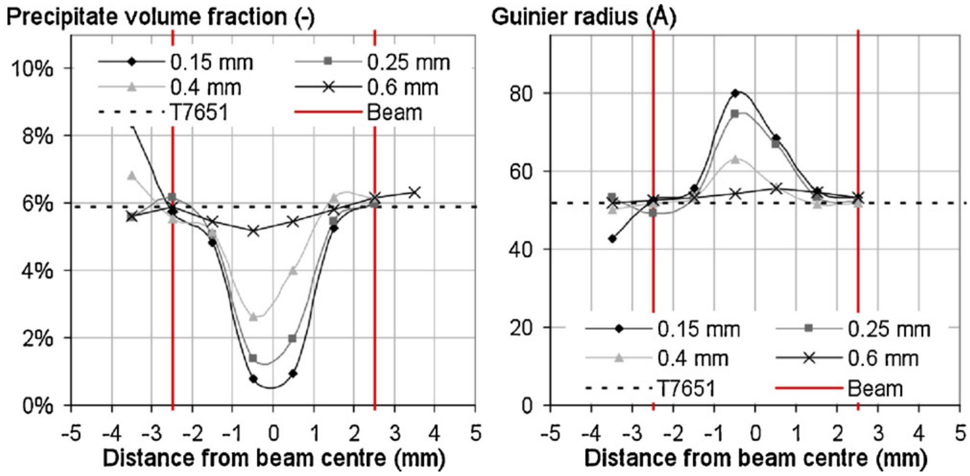

Fig. 7. Line scans for the precipitate volume fraction and the Guinier radius (calculated from the SAXS curves) realised below the laser line #3.

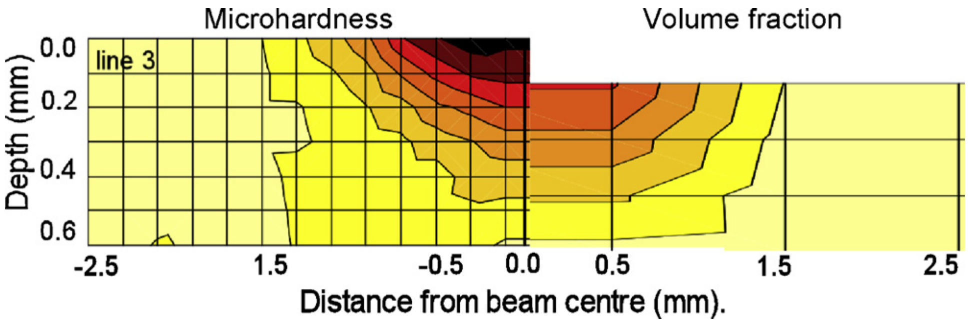

Fig. 8. Comparison between the hardness and volume fraction maps obtained below laser line #3.

where $K^{\infty}_{MgZn_2} = \exp\left((\Delta S_0/k_B) - (\Delta H_0/k_BT)\right)$ is the equilibrium solubility product of the η phase and $R_0 = 3(2\gamma\Omega/k_BT)$ (where γ is the interfacial energy and Ω the mean atomic volume within the precipitate, assumed to be equal to that of the matrix) is the so-called capillarity radius. The factor 3 accounts for the number of atoms in the $MgZn_2$ molecule.

Nucleation was made possible in the model when the supersaturation was large enough (such as after extensive precipitate dissolution and subsequent change of temperature). The nucleation rate (applying to the precipitate size class corresponding to the critical size) was calculated as follows:

$$\frac{dN_n}{dt} = N_0 Z \beta^* \exp\left(\frac{-\Delta G^*}{k_BT}\right)\exp\left(-\frac{\tau}{t}\right) \tag{2}$$

where ΔG^* is the energy barrier for nucleation, N_0 the density of nucleation sites (=$1/\Omega$) and β^{*-1} the critical attachment rate. This duration can be expressed, for one solute i, as:

$$\beta^*_i = \frac{4\pi R^{*2} D_i X^\alpha_i}{a^4} \tag{3}$$

where a is the matrix lattice parameter and X^α_i the (atomic) solute fraction in the matrix. The mean duration β^{*-1} in the presence of two species considers the two constituents of the precipitates, Mg and Zn:

$$\beta^{*^{-1}} = \beta^{-1}_{Mg} + 2\beta^{-1}_{Zn} = \frac{a^4}{4\pi R^{*2}}\left(\frac{1}{D_{Mg}X^\alpha_{Mg}} + \frac{2}{D_{Zn}X^\alpha_{Zn}}\right) \tag{4}$$

In Eq. (2), the second exponential term accounts for the presence of an incubation period:

$$\tau = \frac{1}{2\beta^* Z^2} \quad \text{where} \quad Z = \frac{\Omega}{2\pi R^{*2}}\sqrt{\frac{\gamma}{k_BT}} \tag{5}$$

When calculating the activation barrier for nucleation, we account for the possibility of heterogeneous nucleation through a tuneable proportionality factor α_{het} that can take a value between 0 (no nucleation barrier) and 1 (homogeneous nucleation):

$$\Delta G^* = \alpha_{het}\frac{4}{3}\frac{\pi R_0^2 \gamma}{S^2} \tag{6}$$

where S is the supersaturation factor defined by:

$$S = \ln\left(X^\alpha_{Mg}\right) + 2\ln\left(X^\alpha_{Zn}\right) - \ln K^{\infty}_{MgZn_2} \tag{7}$$

The critical size for nucleation R^*, which was also subsequently the critical radius defining the boundary between the growing and dissolving classes, is calculated as:

$$R^* = \frac{R_0}{S} \tag{8}$$

After accounting for possible nucleation, the behaviour of each of the precipitate size classes is simply determined by the current value of the solid solution using a classical growth equation applied to both diffusing species, e.g. to Mg:

$$\frac{dR}{dt} = \frac{D_{Mg}}{R}\frac{X^\alpha_{Mg} - X^i_{Mg}}{X^p_{Mg} - X^i_{Mg}} \tag{9}$$

The interfacial concentration is determined for each precipitate class using the solute flux compatibility equation resulting from the stoichiometric nature of the precipitates, similarly to [21].

The initial precipitate size distribution corresponding to the T7651 temper was calculated by adjusting a log-normal distribution of ellipsoids to the SAXS scattering, similarly to [27]. Fig. 10 shows the result of the data fitting by the distribution of ellipsoids. The resulting distribution had a mean radius of 44.9 Å, a relative

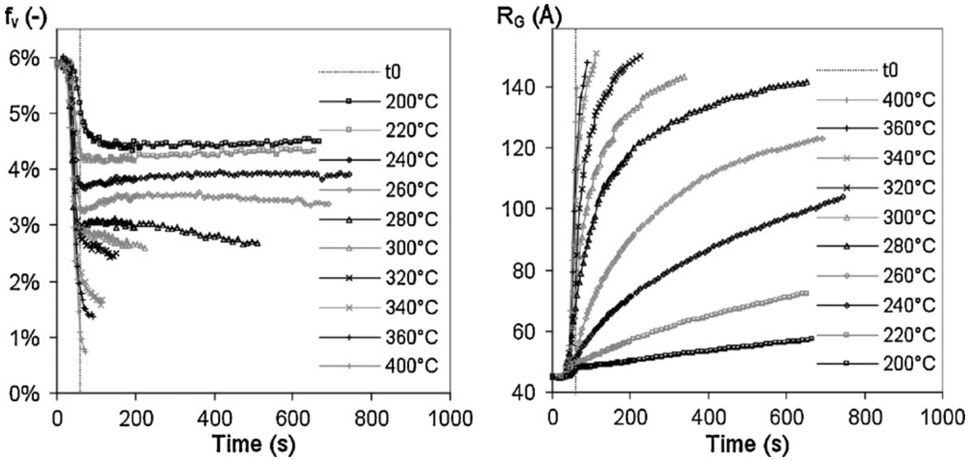

Fig. 9. Evolution of precipitate volume fraction (f_v) and precipitate radius (R_G) during the reversion heat treatments realised at temperatures ranging from 200 to 400 °C.

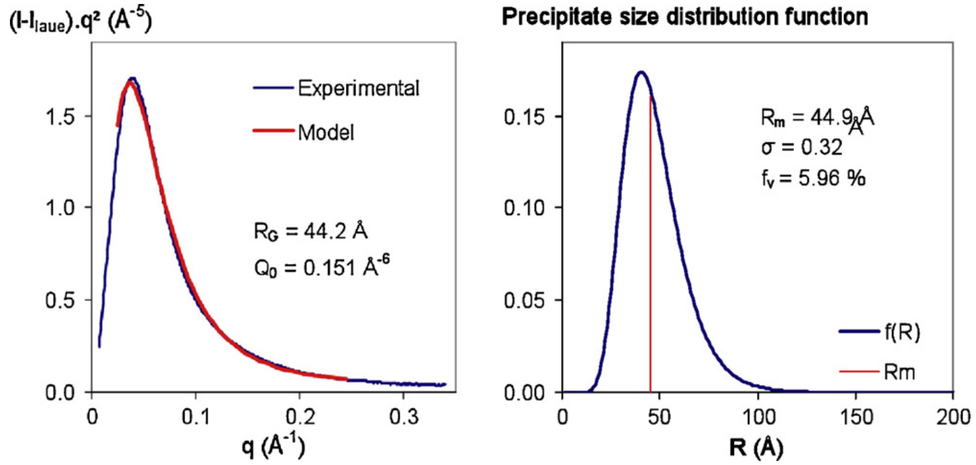

Fig. 10. (Left) Experimental SAXS curve in a Kratky plot vs. the curve obtained by modelling the precipitate size distribution as a distribution of ellipsoids. (Right) Resultant size distribution (precipitate sizes are given as sphere radius of equivalent volume).

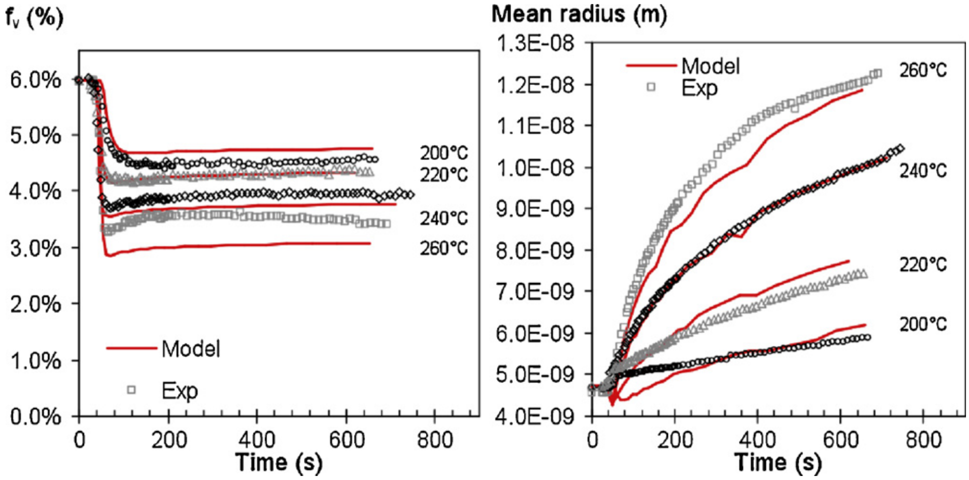

Fig. 11. Comparison between the experimental SAXS reversion behaviour and the model results in the temperature range 200–260 °C.

standard deviation of 0.32 and an aspect ratio of 0.39. This distribution was taken as a starting point for the precipitation modelling, assuming that the precipitates are spherical.

Fig. 11 shows the comparison of the experimental results and the precipitation model in the temperature range 200–260 °C. Above this temperature no reasonable agreement could be found, probably due to extensive heterogeneous precipitation at the reversion temperature. Table 1 shows the model parameters obtained with this fitting procedure. The nucleation parameter was evaluated using separate isothermal ageing measurements that can be found in [28].

A good agreement is reached for the description of the reversion behaviour, both in terms of precipitate size and volume fraction. The next step was to model the ramp heating experiments, which are shown in Fig. 12. Using the same set of parameters, the continuous heating experiments were properly described, with a continuous decrease of the volume fraction and a sharp increase of precipitate size after a critical level of dissolution has happened. Therefore, at this stage the model is able to describe the evolution of the precipitate microstructure during a sudden rise in temperature, and during continuous heating. The next step will be to apply this model to temperature paths predicted by thermal modelling for the laser treatment, and compare the end microstructures with the experimental ones.

7. Thermal modelling

The temperature evolution was computed using a laser beam heat flux model such as presented in [15]. For the finite element model, the specimen was meshed with SHELL131 elements of the ANSYS code. It is a 3-D layered shell element with in-plane and through-thickness thermal conduction capability. The element has four nodes with up to 32 temperature degrees of freedom at each node. Ten layers through the thickness of the 5 mm plate were considered. The mesh was refined in the area near the laser beam, as shown in Fig. 1b.

Table 1
Parameters for the precipitation model. D_{oMg} and D_{oZn} are the pre-exponential factors for the diffusion constants of Mg and Zn. Q_{Mg} and Q_{Zn} are the activation energies for these diffusion constants. The other parameters are defined in the text.

Parameter	D_{oMg}	Q_{Mg}	D_{oZn}	Q_{Zn}	γ	α_{het}	ΔS_o	ΔH_o
Unit	$m^2 s^{-1}$	$kJ mol^{-1}$	$m^2 s^{-1}$	$kJ mol^{-1}$	$J m^{-2}$	–	$kJ mol^{-1} K^{-1}$	$J mol^{-1}$
Value	$1.3e^{-8}$	85.3	$1.3e^{-7}$	85.3	0.5	0.3	59.8	15.8

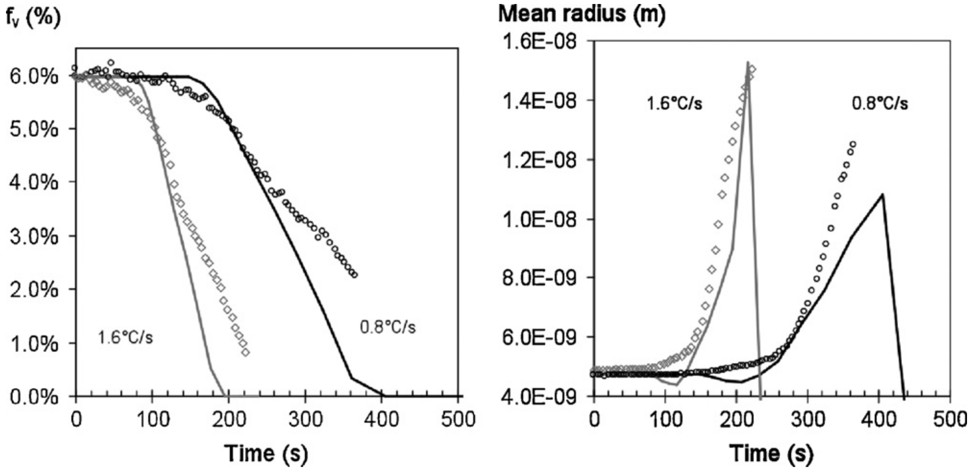

Fig. 12. Comparison between the experimental results from SAXS during continuous heating experiments and the model results.

The heat input was introduced in the finite element model using the following surface heat flux distribution:

$$Q(x,y)=\frac{c\cdot \mathrm{AC}\cdot P}{\pi\cdot r_o^2}\cdot \exp\left(-c\left(\left(\frac{x}{r_o}\right)^2+\left(\frac{y}{r_o}\right)^2\right)\right) \qquad (10)$$

where AC is the laser absorption coefficient of the irradiated surface, P is the laser beam power, r_o is the laser beam radius equal to 2.5 mm for all investigated cases, c is a shape parameter of the heat-flux distribution and x, y, z are the Cartesian coordinates. The above parameters that are required in the laser beam heat flux simulation model can be divided into three groups: process parameters (beam power, diameter, scanning velocity and distance from material), material parameters (thermal conductivity, heat capacity and density) and specimen parameters. This third group includes the specimen geometry but also the material absorption coefficient, which depends mainly on the material surface state (colour and roughness). This last parameter is difficult to determine accurately. For this reason, the temperature distribution for different values of absorption coefficient between 0.1 and 0.2 were calculated and the value of the absorption coefficient was evaluated by an inverse methodology: the experimental precipitation state measured on the laser treated part was compared to the modelled precipitation state, resulting from the computed temperature profile.

An example of the evolution of the temperature distribution on the outer surface of the plate during the 5 successive laser processing lines is shown in Fig. 13. In this case the absorption coefficient (AC) was chosen at 0.10, which generates a maximum temperature of ~420 °C, in the middle of the laser beam. At first sight, one can notice an increase of the mean plate temperature between the first and the last laser lines, from ~25 °C to ~60 °C. This effect will be seen more clearly in the following figures, where more quantitative data will be available.

Fig. 14 shows the evolution of temperature at some relevant locations during the whole laser process: (a) on the surface, in the middle of laser lines 1, 3 and 5 and (b) for different depths in the centre of laser line 1. The temperature at a given point rises sharply when the laser beam approaches. The reached peak temperature, which lies well above the temperature of the T7651 heat treatment (160 °C), is probably high enough to destabilise the precipitates. This stage lasts less than 1 s, after which the temperature goes back to lower values (less than 100 °C) when the laser beam goes away. Then, new temperature increases can be observed when the laser beam goes along the next lines.

The mean plate temperature increases during the whole process, going from room temperature to ~60 °C. As a consequence, the peak temperature from one laser line to another is also observed to rise. There is a high temperature gradient in the depth of the specimen in the near-peak area (see Fig. 15). The temperature profile is very steep and reaches high values in the top surface (in that case: 374 °C), but less than 160 °C in the middle of the plate and even less in the bottom of the plate (5 mm under the top surface). This gradient decreases and disappears very soon after the peak: in less than 1 s, the temperature is homogeneous throughout the plate.

The same calculations were performed with different absorption coefficients of the laser beam into the plate, namely 0.125, 0.15 and 0.20, instead of 0.10. An example of the influence of this parameter is given in Fig. 16. One can notice that the absorption

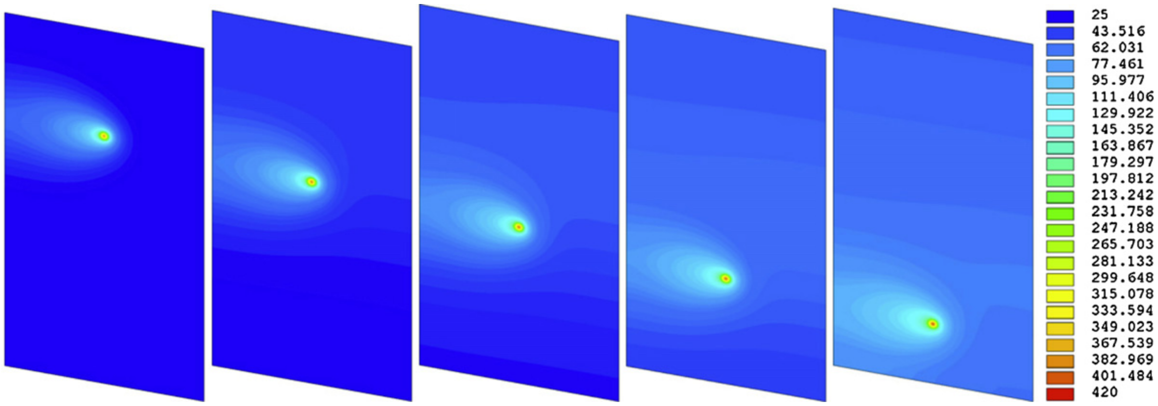

Fig. 13. Predicted temperature distributions at the sample surface during the laser processing for the 5 successive lines (1 to 5 from left to right), with AC = 0.1.

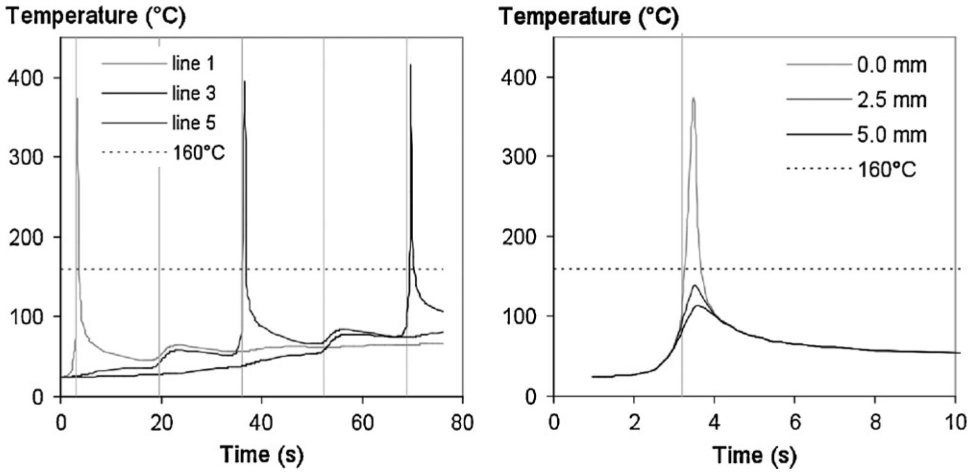

Fig. 14. Temperature profiles predicted in different locations of the plate during the laser processing (with AC = 0.1). (Left) Surface temperatures in the centre of lines 1, 3 and 5 (right) surface temperature compared with those at depths 2.5 mm (middle of the plate) and 5 mm (opposite surface of the plate) for line #1.

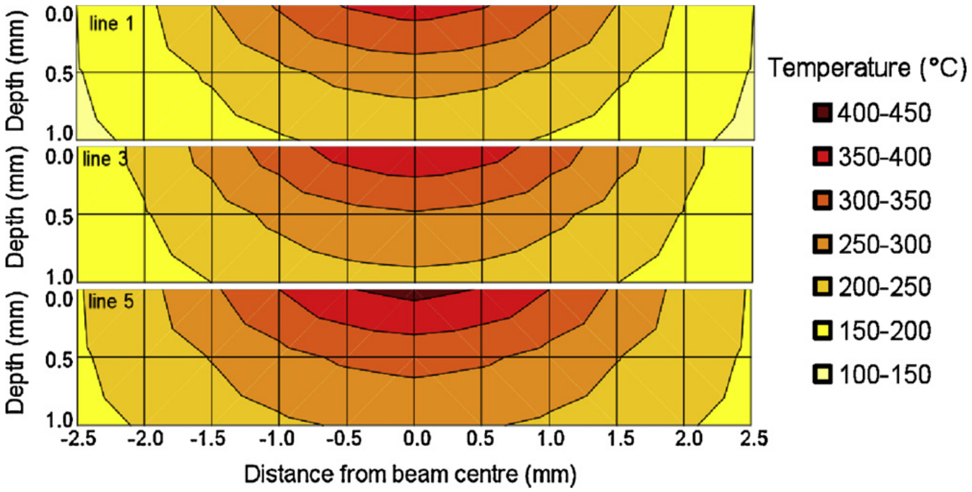

Fig. 15. Numerically predicted spatial distribution (with AC = 0.1) of the maximum temperature experienced in the plate below the lines 1 (top), 3 (middle) and 5 (bottom).

coefficient plays a very significant role on the peak temperature, but also on the average plate temperature. For laser line 5 for instance, the peak temperature varies from 416 °C for AC = 0.10 to 785 °C for AC = 0.20. Such a high temperature would exceed the material fusion temperature, which is in contradiction with our experimental observations.

In order to determine the value of this absorption coefficient more accurately, we applied the thermal fields predicted for different values of AC to the precipitation model with the calibration procedure made above, for a point located 0.5 mm below the surface in the centre of laser line #3. The microstructure study provided the precipitate radius in this location (58 Å) and the residual volume fraction (4%) after laser treatment. Fig. 17 shows the predicted evolution of the microstructure during the laser treatment. The model predicts a sharp drop of volume fraction during the temperature spike, together with a decrease of the precipitate radius. The first point corresponds well with the experimental data, and an absorption coefficient of 0.1 reproduced correctly the final volume fraction. The second point is actually in contradiction with the experimental results, since we have seen before that within the laser lines the precipitate size was actually larger than that of the base material. This can be understood when looking at the initial and final modelled precipitate size distributions as shown in Fig. 18. The model predicts that the precipitate size distribution evolves in two separate directions, with some precipitates remaining at a size

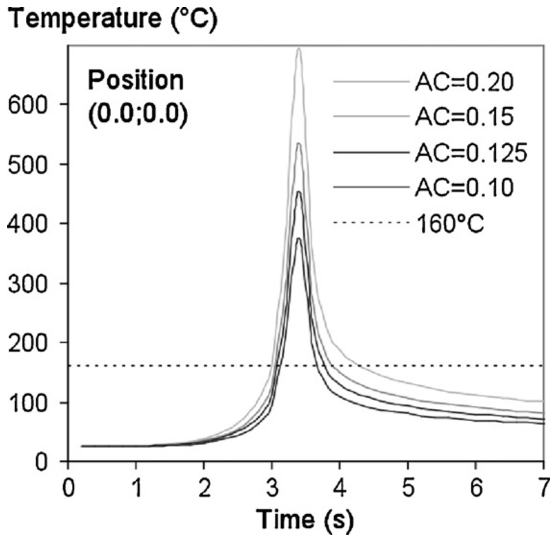

Fig. 16. Influence of the AC (absorption coefficient) parameter of the model on the predicted temperature predicted on the plate surface below the centre of line #1.

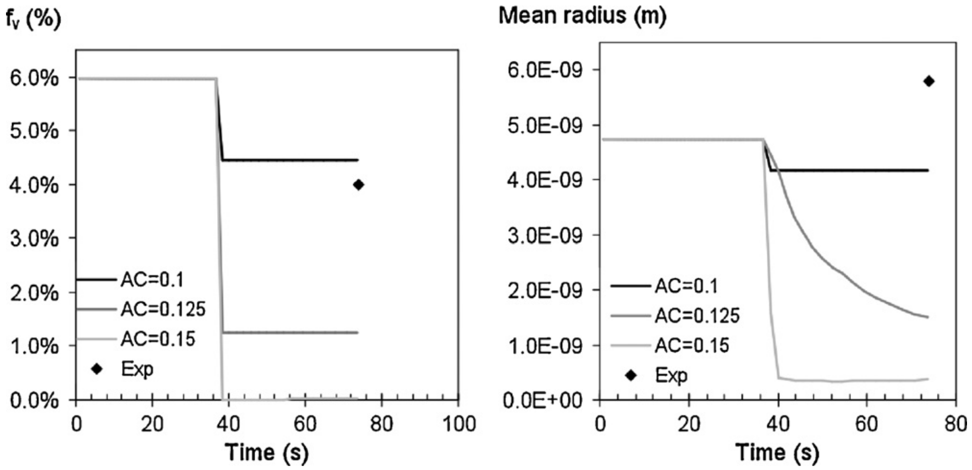

Fig. 17. Microstructure evolution (precipitate volume fraction and radius) predicted by applying the modelled thermal profile predicted to the microstructure model, with the initial state set up for the T7651 temper. Several values of the AC parameter, which result in different temperature profiles, are considered. The experimental point corresponds to the microstructure measured after laser treatment.

comparable to the initial one, and some very fine precipitates that nucleate during the last stages of the heat treatment at low temperature. These fine precipitates represent only a small proportion of the total volume fraction, but shift significantly the measured precipitate radius. Actually, the SAXS experiments were adjusted (in terms of the range of scattering vectors accessible) in order to detect rather large precipitates and were not capable of observing such small precipitates as the model predicts to form in the last stages of the laser treatment. Within this limitation, AC = 0.1 gives reasonable results and this value will be considered from now on.

8. Model prediction of the microstructure and properties maps

The last step of the modelling procedure was to apply the thermal fields predicted by the thermal model with AC = 0.1 to the initial T7651 precipitation microstructure, and compare the end results with the experimental "precipitation maps" obtained from the SAXS measurements. Fig. 19 shows such a comparison for the volume fraction as well as for the precipitate size. For the volume fraction, a very good agreement is obtained, both in terms of the extension of the heat-affected zone, of its shape (width-to-depth ratio), and in terms of the extension of the precipitate dissolution. For the precipitate size, the agreement is not good. As discussed above this is due to the fact that the model predicts some re-precipitation of very fine scale precipitates in the late stages of laser operation, which were not detected by the SAXS experiments.

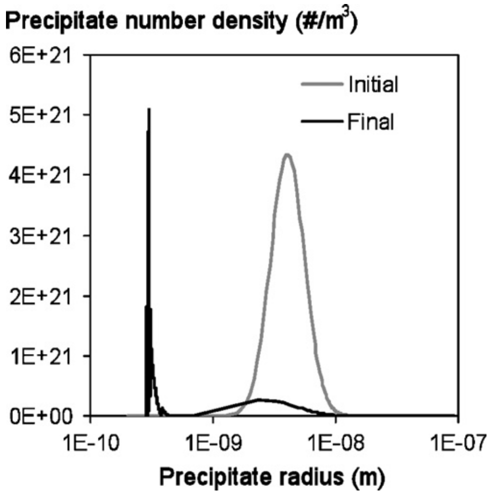

Fig. 18. Precipitate size distributions before the heat treatment (fitted on the SAXS signal) and after the laser treatment corresponding to the conditions of Fig. 17 (predicted by the microstructure model).

Now that the precipitate microstructure maps are available, it is possible to apply a precipitation strengthening model to this data to compare with the microhardness maps. We applied a classical approach combining shearing and by-passing mechanisms for the precipitate–dislocations interactions. The details of the model and how its parameters were fitted with SAXS and yield strength data along various heat treatments can be found in [28].

Two strategies were applied to model the hardness distribution through the cross section below the laser line #3. (i) The strengthening model was applied to the microstructure data measured by SAXS; (ii) the strengthening model was applied to the microstructures predicted by the thermal and precipitation models. Fig. 20 shows the two calculated microhardness maps. The one calculated using the full model provides a very accurate description of the hardness distribution within the cross-section, whereas the hardness map calculated from the experimental distribution of precipitate sizes overestimates the softening due to the laser process. This difference is actually the result of the lack of the fine scale precipitates in the measured microstructure maps, whereas these precipitates are present in the modelled maps. Thus it is likely that these precipitates formed during the last stages of the laser treatment (where the plate is at a temperature close to 70 °C) are actually present in the microstructure, and help to reduce the laser-induced softening. It is a limitation of the present study that we have not an experimental proof of their presence, nor of their nature. Since these precipitates are likely formed below 100 °C, they are certainly Guinier Preston (GP) zones. These particles could have been detected by a proper SAXS set-up measuring much wider scattering angles, or by other techniques such as Atom Probe Tomography. However, one must consider the fact that the microstructure directly following the laser treatment is not stable and evolves rapidly at room temperature, which makes it more difficult to study. In order to account properly for them in the model, one would have to calibrate separately a precipitation model for GP zones and apply it to the cooling stage of the thermal path induced by the laser treatment.

The potential for further reduction of laser-induced softening by natural ageing has been evaluated after 1 year of natural ageing,

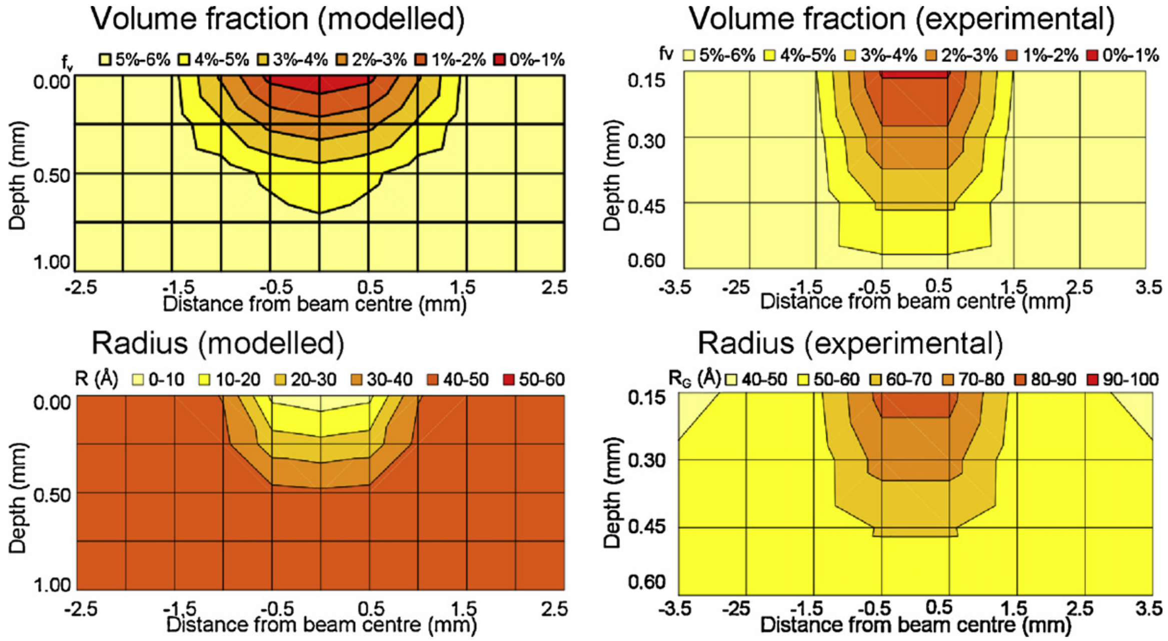

Fig. 19. Comparison between the experimental and modelled maps for volume fraction and radius of the precipitates below line #3. Note that the scales of the experimental and model maps are different.

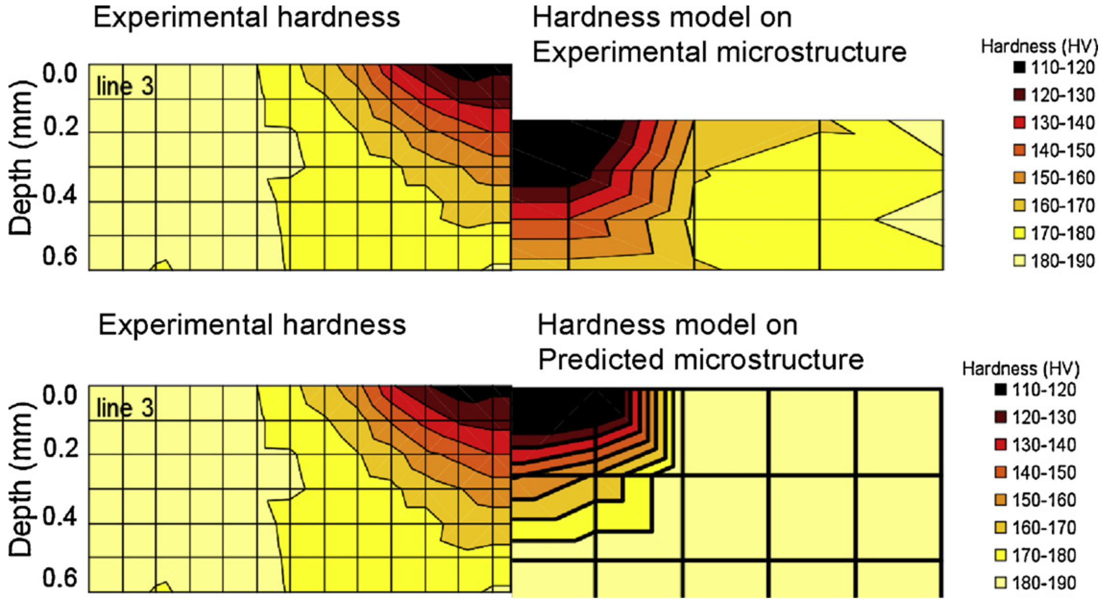

Fig. 20. Comparison between experimental and predicted hardness maps using the hardness model either on the experimental microstructure maps or on the microstructure maps predicted using the thermal + microstructure models.

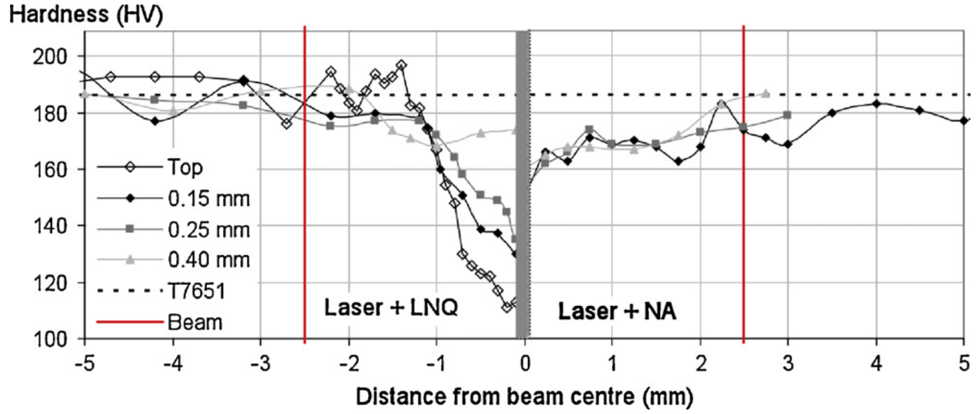

Fig. 21. Microhardness profiles measured at different depths below the sample surface for the line #3, in the as-laser treated material (left), and after 1 year of natural ageing (right).

as shown in Fig. 21. The hardness at three distances from the plate surface were measured in the naturally aged plate, and compared to the values measured on samples kept in liquid nitrogen after the laser treatment until the hardness measurements. The natural ageing actually provides a substantial amount of hardness recovery, which is consistent with the discussion on the hardness immediately after the laser treatment. After one year, the maximum level of observed softening is only of about 30 HV against 80 HV before natural ageing.

9. Discussion and conclusions

The present study aimed at reaching a comprehensive understanding of the effect of a thermal laser treatment on the precipitate microstructure and resulting properties of a T7651 AA7449 aluminium alloy. By mapping the microstructure and applying successive models for the temperature fields, their influence on the precipitate microstructure and the link between this microstructure and the properties, it has been possible to assess the extension of the heat-affected zone and to gain insight into the mechanisms prevailing during the laser treatment:

(i) The very short temperature spike caused by the laser treatment induces mostly precipitate dissolution, however several lower temperature processes have been shown to be influential to the material response. When multiple passes are performed on a single plate, the average temperature of the plate increases substantially, which causes a rise in the peak temperature experienced during the last passes (and in turn increases the amount of precipitate dissolution). But it also causes the precipitation of new very fine particles (probably GP zones) in the dissolved zones of the first passes; additional work is necessary to assess the exact nature and characteristics (size, volume fraction, hardening potential) of these fine particles.

(ii) The investigated laser treatment results in a very significant precipitate dissolution in the first 500 μm below the surface, together with a modification of the precipitate size. Although the very small precipitates that form during the late stages of the laser treatment and during natural ageing compensate partly the mechanical loss, this microstructure change should not be overlooked when applying such treatments to correct part distortions in aerospace components. Its influence on various properties such as buckling, fracture toughness or corrosion resistance should be assessed.

(iii) The microstructure and properties maps can be reproduced by a fully integrated model including thermal modelling and precipitation modelling. One limitation of the current integrated model is that it does not account properly for the precipitation of the fine GP zones upon cooling. Within this limitation, such an integrated model can be a useful tool for process optimisation.

Acknowledgements

Dr. F. Bley and the staff of BM02-D2AM beamline is thanked for technical help with the experiments. This work was carried out in the COMPACT project which is a collaboration between Airbus UK (Project Co-ordinator), Alcan – Centre de Recherches de Voreppe, Limerick University, University of Bristol, Enabling Process Technologies, University of Hannover, EADS Germany, University of Patras, Alenia Aeronautica, Ultra RS, Institut Polytechnique de Grenoble and the University of Sheffield. The project was jointly funded by the European Union Framework 6 initiative and the project partners. One of the authors (AD) wishes to acknowledge the support of the European Research Council for support in the framework of the NEMOLight Marie Curie International Outgoing Fellowship within the 7th European Community Framework Programme. Partial support of "Agence Nationale de la Recherche" on CONTRAPRECI project 06-BLAN-0205 is gratefully acknowledged.

References

[1] J.E. Rankin, M.R. Hill, L.A. Hackel, Mater. Sci. Eng. A349 (2003) 279–291.
[2] O. Hatamleh, J. Lyons, R. Forman, Int. J. Fatigue 29 (2007) 421–434.
[3] O. Hatamleh, Mater. Sci. Eng. A492 (2008) 168–176.
[4] O. Hatamleh, Int. J. Fatigue 31 (2009) 974–988.
[5] O. Hatamleh, M. Hill, S. Forth, D. Garcia, Mater. Sci. Eng. A519 (2009) 61–69.
[6] O. Hatamleh, P.M. Singh, H. Garmestani, J. Mater. Eng. Perform. 18 (2009) 406–413.
[7] A.T. DeWald, M.R. Hill, J. Strain Anal. Eng. 44 (2009) 1–11.
[8] C.A. Rodopoulos, A.T. Kermanidis, E. Statnikov, V. Vityazev, O. Korolkov, J. Mater. Eng. Perform. 16 (2007) 30–34.
[9] J. Noordhuis, J.T.M. Dehosson, Acta Metall. Mater. 41 (1993) 1989–1998.
[10] T.M. Yue, L.J. Yan, C.P. Chan, Appl. Surf. Sci. 252 (2006) 5026–5034.
[11] Z. Ji, S.C. Wu, J. Mater. Process. Technol. 74 (1998) 89–95.
[12] K.C. Chan, J. Liang, J. Mater. Process. Technol. 100 (2000) 214–218.
[13] Z. Hu, M. Labudovic, H. Wang, R. Kovacevic, Int. J. Mach. Tool. Manuf. 41 (2001) 589–607.
[14] M. Geiger, M. Merklein, M. Pitz, J. Mater. Process. Technol. 151 (2004) 3–11.
[15] G.N. Labeas, J. Mater. Process. Technol. 207 (2008) 248–257.
[16] F. Heymes, B. Commet, B. DuBost, P. Lassince, P. Lequeu, G.M. Raynaud, in: T. Bains, D.S. MacKenzie (Eds.), 1st International Non-Ferrous Processing and Technology Conference, ASM International, OH, USA, 1997, pp. 249–255.
[17] J. Lendvai, Mater. Sci. Forum 217–222 (1996) 43–56.
[18] M. Nicolas, A. Deschamps, Metall. Mater. Trans. 35A (2004) 1437–1448.
[19] M. Dumont, A. Steuwer, A. Deschamps, M. Peel, P.J. Withers, Acta Mater. 54 (2006) 4793–4801.
[20] A. Deschamps, S. Ringeval, G. Texier, L. Delfaut-Durut, Mater. Sci. Eng. A517 (2009) 361–368.
[21] M. Nicolas, A. Deschamps, Acta Mater. 51 (2003) 6077–6094.
[22] G. Kostorz, J. Appl. Crystallogr. 24 (1991) 444–456.
[23] M. Dumont, W. Lefebvre, B. Doisneau Cottignies, A. Deschamps, Acta Mater. 53 (2005) 2881–2892.
[24] A. Deschamps, M. Perez, C. R. Phys. 11 (2010) 236–244.
[25] M. Perez, E. Courtois, D. Acevedo, T. Epicier, P. Maugis, Philos. Mag. Lett. 87 (2007) 645–656.
[26] M. Perez, M. Dumont, D. Acevedoreyes, Acta Mater. 56 (2008) 2119–2132.
[27] F. Perrard, A. Deschamps, F. Bley, P. Donnadieu, P. Maugis, J. Appl. Crystallogr. 39 (2006) 473–482.
[28] G. Fribourg, Precipitation and Plasticity Couplings in a 7xxx Aluminium Alloy: Application to Thermomechanical Treatments for Distortion Correction of Aerospace Components, PhD Thesis, Institut Polytechnique de Grenoble, France, 2009.